

---

# Wavelet Flow: Fast Training of High Resolution Normalizing Flows

---

Jason J. Yu<sup>1,3</sup>, Konstantinos G. Derpanis<sup>2,4,5</sup> and Marcus A. Brubaker<sup>1,3,5</sup>

<sup>1</sup>Department of Electrical Engineering and Computer Science, York University, Toronto

<sup>2</sup>Department of Computer Science, Ryerson University, Toronto

<sup>3</sup>Borealis AI, <sup>4</sup>Samsung AI Centre Toronto, <sup>5</sup>Vector Institute

jyyu@eecs.yorku.ca   kostas@cs.ryerson.ca   mab@eecs.yorku.ca

## Abstract

Normalizing flows are a class of probabilistic generative models which allow for both fast density computation and efficient sampling and are effective at modelling complex distributions like images. A drawback among current methods is their significant training cost, sometimes requiring months of GPU training time to achieve state-of-the-art results. This paper introduces *Wavelet Flow*, a multi-scale, normalizing flow architecture based on wavelets. A Wavelet Flow has an explicit representation of signal scale that inherently includes models of lower resolution signals and conditional generation of higher resolution signals, *i.e.*, super resolution. A major advantage of Wavelet Flow is the ability to construct generative models for high resolution data (*e.g.*,  $1024 \times 1024$  images) that are impractical with previous models. Furthermore, Wavelet Flow is competitive with previous normalizing flows in terms of bits per dimension on standard (low resolution) benchmarks while being up to  $15\times$  faster to train.

## 1 Introduction

Here we introduce *Wavelet Flow*, a multi-scale, conditional normalizing flow architecture based on wavelets. Wavelet Flows are not only fast when sampling and computing probability density, but are also efficient to train even with high resolution data. Further, the model has an explicit, wavelet-based, representation of scale which, among other benefits, includes consistent models of low resolution signals and conditional generation of higher resolutions. Wavelet Flow is applicable to any suitably structured data domain including audio, images, videos, and 3D scans. Our experiments focus on images as they are the most widely considered domain. The results demonstrate that Wavelet Flow is competitive with state-of-the-art normalizing flows on (typically low resolution) standard benchmarks while being significantly more efficient to train, *e.g.*, up to 15 times more in some cases. Further, we introduce the first normalizing flow model trained on high resolution images, *i.e.*,  $1024 \times 1024$ .

Normalizing flows are a class of probabilistic generative models which enable fast density computation and efficient sampling [9, 10, 27, 37]. They have also been shown to be effective at modelling complex distributions like images [25]. However, current approaches come with a significant computational cost, typically requiring months of GPU training time to achieve state-of-the-art results. This is partly driven by the requirement that normalizing flows be invertible and preserve dimensionality. Dinh et al. [10] identified this challenge and introduced a form of multi-scale flow which uses an identity transform on increasing subsets of dimensions to reduce computation. As an addition to this multi-scale flow, Ardizzone et al. [2] further proposed using a Haar wavelet transform for reshaping and reducing spatial resolution within a normalizing flow. In either case, the structure progressively limits the complexity of the transformation in certain dimensions but neither exposes nor exploits the natural scale structure in the signal itself. In contrast, Wavelet Flow uses a wavelet transformation

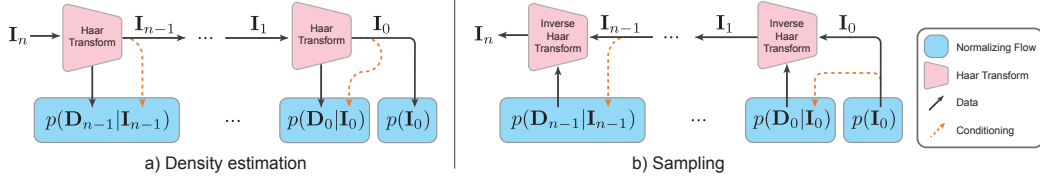


Figure 1: The architecture of a Wavelet Flow during (a) density estimation, and (b) sampling. The normalizing flows at each level (blue) can be trained independently from each other for easy parallelization. Sampling is performed in a coarse-to-fine manner, where each flow is conditioned (orange) on the lower resolution image.

[35] of the data that naturally exposes its inherent scale structure. This transformation enables a factorization of the distribution across scale and a novel conditional architecture, where coarse structure is generated first with the generation of increasingly fine details following, conditioned on the coarser structure.

The conditional structure of Wavelet Flow is reminiscent of autoregressive models [44, 42]. In these methods, conditioning is defined by an arbitrary pixel ordering, whereas the conditioning in Wavelet Flow is global but resolution limited. van den Oord et al. [44] also described a multi-scale variant of the PixelRNN that generates a full higher resolution image conditioned on a lower resolution input; however, this structure does not limit the conditional generation to the added content of the higher resolution image. Hence such a model can only be used for generation and does not allow for inference, *i.e.*, computing the probability density of a high resolution image. In contrast, Wavelet Flow conditionally generates only the detail coefficients of the wavelet representation at each scale and allows for inference of the probability density of an image at each modelled scale. Reed et al. [39] described a multi-scale autoregressive model, which consists primarily of an alternative ordering of the pixels rather than a direct representation of image scale.

In this work, we introduce the use of a multi-scale signal decomposition in normalizing flows. In general, multi-scale representations have been an area of significant interest in computer vision for decades [6, 36, 47, 5, 7, 28, 1, 34, 30, 31, 4]. Their use is driven by the inherent scale structure that exists in natural signals [30]. The Fourier basis [3] is perhaps the best known multi-scale decomposition and is both invertible and orthonormal; however, its global basis functions render modelling in the Fourier domain challenging. Gaussian and Laplacian pyramids [6, 5, 7, 1, 30, 31] provide an overcomplete but local representation for efficient coding and scale-sensitive representations. Mallat [34] showed that wavelets can be used as a multi-scale, orthogonal, and local representation of discrete signals, which have since been widely used for a variety of applications including compression and restoration. Here, we show how the orthogonality and spatial locality of wavelets make them uniquely well suited for use in normalizing flows.

Multi-scale image representations have also been explored in other forms of generative modelling, including generative adversarial networks (GANs) [12] and variational auto-encoders (VAEs) [26]. Denton et al. [8] proposed a hierarchical GAN consisting of a sequence of conditional GANs which generate the residual images of a Laplacian pyramid [5] representation. This is similar to our method which conditionally models the detail coefficients of each scale of a wavelet representation. However, the Laplacian pyramid is an overcomplete representation making it unsuitable for use in a normalizing flow. Various subsequent works [49, 22, 45, 21, 50, 43] also follow a stage-wise multi-scale image generation approach but forego the residual modelling and directly generate higher resolution images given lower resolutions inputs. PixelVAE [14] uses a hierarchical structure in their latent space but does not explicitly represent signal scale. Razavi et al. [38] extended the vector quantized variational autoencoder (VQ-VAE) model [44], by introducing scale dependent (discrete) latent codes, independently capturing local (*e.g.*, texture) and more global image aspects (*e.g.*, objects). Image generation is realized by a multi-stage PixelCNN [44] capturing the priors over the various scale-dependent latent maps. Dorta et al. [11] used a Laplacian pyramid with conditional VAEs in a manner similar to Wavelet Flow but primarily focus on image editing applications.

**Contributions** We propose the use of wavelets in normalizing flows. Orthonormal wavelets produce a multi-scale signal representation and, as we show, are convenient for use as part of a normalizing flow. We show that the distribution over a wavelet representation of a signal has a natural coarse-to-



fine conditional decomposition, which has a number of benefits including efficient and highly parallel training. Other benefits we explore include embedded, self-consistent distributions of lower resolution signals, and conditional generation of higher resolution signals (*i.e.*, super resolution). We also exploit this decomposition to introduce a novel sampling algorithm to draw samples from an annealed version of the resulting distribution. We apply the Wavelet Flow architecture to images, including  $1024 \times 1024$  high resolution imagery which has not been previously modeled with normalizing flows. Compared against other normalizing flows on standard datasets, we demonstrate that Wavelet Flow has competitive performance while being up to  $\sim 15\times$  faster to train. Code for Wavelet Flow is available at the following project page: <https://yorkucvil.github.io/Wavelet-Flow>.

## 2 Methods

In this section, the specifics of Wavelet Flow are described. To begin, wavelets are introduced (Sec. 2.1), then normalizing flows are briefly described (Sec. 2.2). Next, we describe how wavelets are used with normalizing flows to construct a Wavelet Flow (Sec. 2.3).

### 2.1 Wavelets

Wavelets are a multi-scale decomposition of a signal similar in concept to a Fourier basis representation. While a Fourier basis is global in nature, wavelets are constructed to be localized, meaning that the value of a wavelet coefficient reflects the structure of the signal in a local region. This is particularly beneficial as modern deep learning architectures generally, including normalizing flows, are well tailored to spatially structured signal representations due to the widespread use of convolutional operations. Here, we briefly introduce wavelets; see [35] for a thorough introduction.

Consider an image  $\mathbf{I} \in \mathbb{R}^{2^n \times 2^n \times C}$ . The discrete wavelet transform is constructed recursively as

$$\mathbf{I}_{i-1} = h_l(\mathbf{I}_i) \text{ and } \mathbf{D}_{i-1} = h_d(\mathbf{I}_i), \quad (1)$$

where  $\mathbf{D}_{i-1} \in \mathbb{R}^{2^{i-1} \times 2^{i-1} \times 3C}$  are the detail coefficients at level  $i-1$ ,  $h_l(\mathbf{I})$  applies the wavelet’s low-pass filter (channel-wise),  $h_d(\mathbf{I})$  applies the wavelet’s high-pass filters (channel-wise), and both  $h_l(\mathbf{I})$  and  $h_d(\mathbf{I})$  use a stride of two, *i.e.*, spatial downsampling the result by a factor of two. The wavelet transform is invertible and the original image can be recovered recursively by

$$\mathbf{I}_i = h^{-1}(\mathbf{I}_{i-1}, \mathbf{D}_{i-1}), \quad (2)$$

where  $h^{-1}$  is the inverse wavelet transform [35]. Applying the wavelet transform recursively until level 0 yields a complete representation of the image, where  $\mathcal{H}(\mathbf{I}) = (\mathbf{I}_0, \mathbf{D}_0, \mathbf{D}_1, \mathbf{D}_2, \dots, \mathbf{D}_{n-1}) \in \mathbb{R}^{C2^{2n}}$  denotes the full wavelet transformation of an image. Note that  $\mathcal{H}(\mathbf{I})$  has the same total dimensionality as  $\mathbf{I}$ . This representation decomposes the content of the image into a range of scales while retaining the dimensionality. At the coarsest scale,  $\mathbf{I}_0 \in \mathbb{R}^{1 \times 1 \times C}$  represents the average intensity per channel and  $\mathbf{D}_0 \in \mathbb{R}^{1 \times 1 \times 3C}$  represents the global variations. At the finest scale,  $\mathbf{D}_{n-1} \in \mathbb{R}^{2^{n-1} \times 2^{n-1} \times 3C}$  represents local variations.

There are many wavelets which have been designed and could be applied here. For Wavelet Flow we choose to use an orthonormal wavelet as described below. For simplicity, a Haar wavelet [15, 35] is used; however, any orthonormal wavelet could be used. Haar wavelets are fast and simple to apply and use only  $2 \times 2$  filters. Additional details for the Haar transformation are available in Appendix C. Exploration of other wavelets remains a direction for future work.

### 2.2 Normalizing Flows

Normalizing Flows are an application of the change of variables formula for probability density estimation. We briefly introduce the core elements here, but for a full review, see [27, 37]. If  $\mathbf{X}$  is a random variable with values  $\mathbf{x} \in \mathbb{R}^D$  then the density function of  $\mathbf{X}$  can be written as

$$p_{\mathbf{X}}(\mathbf{x}) = p_{\mathbf{Z}}(\mathbf{f}_{\theta}(\mathbf{x})) |\det \mathbf{J}_{\theta}(\mathbf{x})|, \quad (3)$$

where  $\mathbf{Z}$  is a random variable which takes on values  $\mathbf{z} \in \mathbb{R}^D$ , with probability density function  $p_{\mathbf{Z}}(\mathbf{z})$ , and with a known distribution which we will assume to be Normal with mean 0 and unit variance.  $\mathbf{f}_{\theta}$  is an invertible, differentiable function parameterized by  $\theta$ .  $\mathbf{J}_{\theta} = \frac{\partial \mathbf{f}_{\theta}}{\partial \mathbf{x}}$  is the Jacobian of  $\mathbf{f}_{\theta}$ . Learning

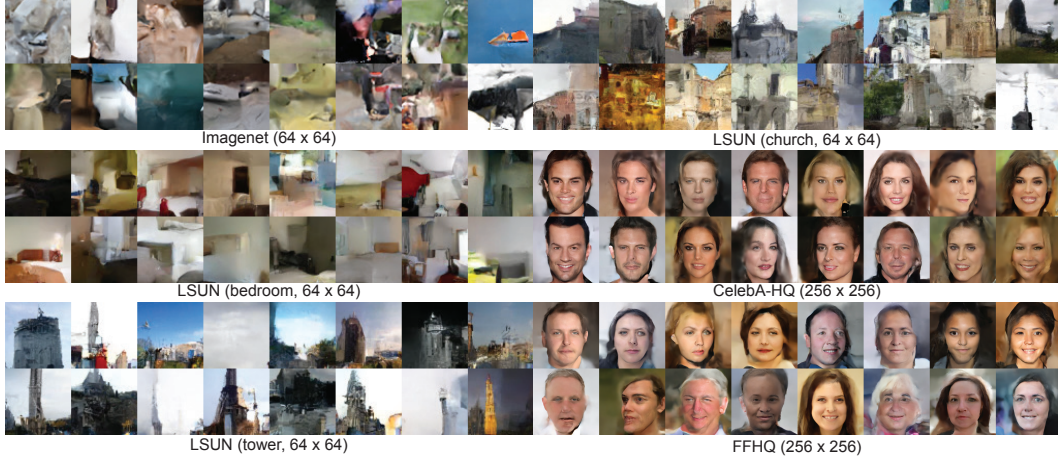


Figure 2: Wavelet Flow samples drawn using MCMC with  $T = 0.97$ .

in normalizing flows consists of optimizing the parameters  $\theta$  to maximize the log likelihood of a set of observations. The resulting distribution can be easily sampled from by drawing samples  $\mathbf{z} \sim p_{\mathbf{Z}}(\mathbf{z})$  and then applying the inverse transformation to yield  $\mathbf{x} = \mathbf{f}_{\theta}^{-1}(\mathbf{z})$ .

The core challenge is constructing invertible and differentiable functions which are also efficient to compute and have easily computable Jacobian determinants. Two widely used functions are *affine* [10] and *additive* [9] *coupling* layers. Affine coupling layers split the input into two disjoint subsets,  $\mathbf{x} = (\mathbf{x}^A, \mathbf{x}^B)$ , and applies the transformation  $\mathbf{f}_{\theta}(\mathbf{x}) = (\mathbf{x}^A, s_{\theta}(\mathbf{x}^A) \odot \mathbf{x}^B + \mathbf{t}_{\theta}(\mathbf{x}^A))$ , where  $\odot$  denotes element-wise multiplication, and  $s_{\theta}(\mathbf{x}^A)$  and  $\mathbf{t}_{\theta}(\mathbf{x}^A)$  are arbitrary functions, typically deep networks of some form, called *coupling networks*. The Jacobian determinant of an affine coupling layer is simply the product of the values of  $s_{\theta}(\mathbf{x}^A)$ , and its inverse is straightforward. An additive coupling layer is simply an affine coupling layer without the scaling operation, *i.e.*,  $\mathbf{f}_{\theta}(\mathbf{x}) = (\mathbf{x}^A, \mathbf{x}^B + \mathbf{t}_{\theta}(\mathbf{x}^A))$ , and has unit Jacobian determinant.

### 2.3 Wavelet Flow

To derive Wavelet Flow, we apply the change of variables to arrive at a distribution of the wavelet coefficients. Specifically,  $p(\mathbf{I}) = p(\mathcal{H}(\mathbf{I})) |\det \frac{\partial \mathcal{H}}{\partial \mathbf{I}}|$ , where we drop the random variable subscripts for clarity. To easily calculate the determinant of the transform, we require that the selected wavelet is orthonormal<sup>1</sup> and hence  $|\det \frac{\partial \mathcal{H}}{\partial \mathbf{I}}| = 1$ . One can now apply the product rule of probability to conditionally factorize the distribution, giving

$$p(\mathbf{I}_n) = p(\mathbf{I}_0) \prod_{i=0}^{n-1} p(\mathbf{D}_i | \mathbf{I}_i), \quad (4)$$

where each  $\mathbf{I}_i$  is constructed using the inverse wavelet transform. In other words, instead of modelling the entire image directly, a Wavelet Flow models the distribution of detail coefficients, conditioned on the lower resolution image. Each conditional distribution of detail coefficients,  $p(\mathbf{D}_i | \mathbf{I}_i)$ , and distribution of average intensity,  $p(\mathbf{I}_0)$ , is constructed using a normalizing flow. Note that inherent in this structure are distributions of all coarser resolution images, *e.g.*,  $p(\mathbf{I}_k) = p(\mathbf{I}_0) \prod_{i=0}^{k-1} p(\mathbf{D}_i | \mathbf{I}_i)$  for all  $k \leq n$ . Hence, a Wavelet Flow model trained at a higher resolution can be used as a model of lower resolution images. The general structure of a Wavelet Flow is shown in Fig. 1 and the specific normalizing flow architecture used for these distributions is described in Sec. 3.

<sup>1</sup>As commonly implemented, the Haar wavelet filters are often unnormalized and hence orthogonal but not orthonormal. This can be rectified by a suitable rescaling.

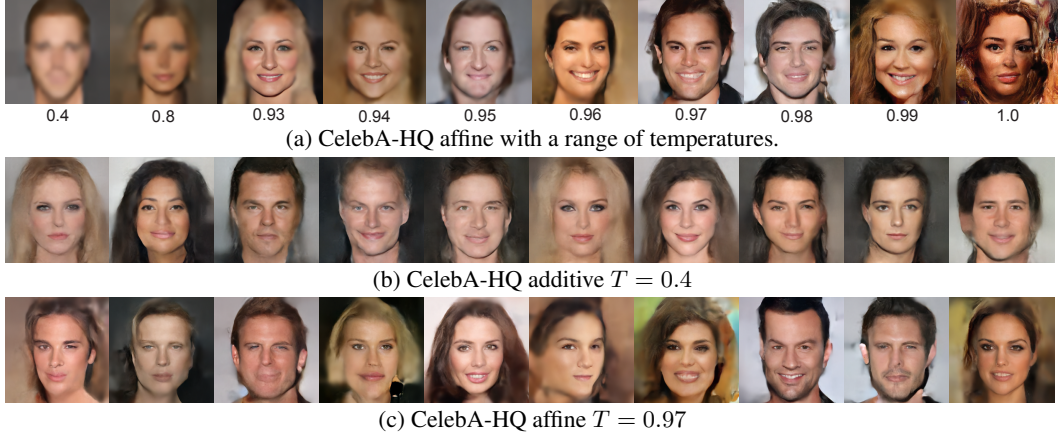


Figure 3: Annealed samples from additive and affine Wavelet Flows on CelebA-HQ.

**Training** Similar to other normalizing flow models, a Wavelet Flow is trained by maximizing the log likelihood. Specifically, we seek to maximize the sum of

$$\log p(\mathbf{I}) = \log p(\mathbf{I}_0) + \sum_{i=0}^{n-1} \log p(\mathbf{D}_i | \mathbf{I}_i) \quad (5)$$

over a set of sample images. This reveals a significant advantage of a Wavelet Flow: the conditional distribution of detail coefficients for each level can be trained *independently*. This makes training more efficient, as it is easily parallelized with no communication overhead, gradient checkpointing or approximations, and the individual distributions are generally smaller and simpler, *i.e.*, they describe lower-dimensional distributions making them easier to fit in limited GPU memory.

**Sampling** Sampling from a Wavelet Flow starts with  $\mathbf{I}_0 \sim p(\mathbf{I}_0)$  and proceeds recursively with

$$\mathbf{D}_{i-1} \sim p(\mathbf{D}_{i-1} | \mathbf{I}_{i-1}) \text{ and } \mathbf{I}_i = h^{-1}(\mathbf{I}_{i-1}, \mathbf{D}_{i-1}), \quad (6)$$

where sampling from each distribution is simply sampling from the corresponding normalizing flow, *i.e.*, sampling from the base distribution of that flow and applying its inverse flow transformation. However qualitative results in normalizing flow papers (*e.g.*, [25, 33]) are typically produced from an annealed distribution  $\propto p(\mathbf{I})^{1/T^2}$  with  $T < 1$  a temperature parameter. Annealing tightens the distribution around its modes and reduces the amount of spurious samples along with limiting sample diversity. If the normalizing flow has a constant Jacobian determinant term (*e.g.*, it consists only of additive coupling layers) then  $p(\mathbf{I})^{1/T^2} \propto p_{\mathbf{Z}}(\mathbf{f}(\mathbf{I}))^{1/T^2}$  and hence samples can be drawn from a Gaussian distribution with its standard deviation scaled by  $T$  and applying the inverse of the flow transformation. This approach does not work with more general flows including, *e.g.*, the affine coupling flows used here. Consequently, previous approaches resort to restrictive models with additive couplings when annealing the distribution for qualitative evaluation while using more expressive models with affine couplings for quantitative evaluation. In this work, we opt to use a single model with affine couplings for both quantitative and qualitative evaluation.

To sample from an annealed flow with affine couplings, we apply Markov Chain Monte Carlo (MCMC) to the annealed, unnormalized distribution  $p(\mathbf{I})^{1/T^2}$ . Specifically, we use the No-U-Turn Sampler (NUTS) algorithm [18, 29] to generate samples. However, the high dimensionality of images can make this expensive. A Wavelet Flow allows us to accelerate sampling by running MCMC separately at each scale and using the resulting samples to condition the next scale. This enables a more efficient sampling due to the lower dimensionality of each scale distribution. For full details of the MCMC approach, see Appendix B.

### 3 Experimental Evaluation

As described in Section 2, the distributions  $p(\mathbf{D}_i | \mathbf{I}_i)$  and  $p(\mathbf{I}_0)$  are constructed using normalizing flows. Specifically, a Glow architecture [25] is used with slight modifications. Since wavelets are



Figure 4: Wavelet Flow samples at  $1024 \times 1024$  on CelebA-HQ (left) and FFHQ (right) with  $T = 0.97$ .

used to decompose the image at multiple scales, the multi-scale squeeze/split architecture from [10] is not used. For the conditional flows, the lower resolution image is concatenated to the input of each coupling network. Learning a conditional transformation of base distributions [46] was explored but not found to improve performance. The coupling networks use a residual architecture with a final zero initialized convolutional layer as in [25].

Training is done using the same Adamax optimizer [24] as in [25]. The architecture of the flow is fully convolutional, and patch-wise training is used for the highest resolution conditional distributions. In cases where overfitting is observed, early stopping is applied based on a held-out validation set. These implementation choices allow for distributions to be trained using a batch-size of 64 without gradient checkpointing on a single NVIDIA TITAN X (Pascal) GPU.

For evaluation baselines, we consider RealNVP [10] and Glow [25] with uniform dequantization for all approaches. Comparison against these methods is only possible on lower resolution datasets as training on high resolution datasets is impractical. We note that improved architectures for a Wavelet Flow remains a direction of future work and could exploit newer flow architectures (*e.g.*, MaCow [33], Flow++ [17], and SoS Flow [20]) and alternative dequantization schemes [17, 19]. Hyper-parameters are set to produce models with parameter counts similar to but not exceeding those of Glow [25] to enable a fair comparison. This requires per-dataset tuning as other approaches used dataset specific architectures. Parameter counts and specific hyper-parameter choices can be found in Appendix C.

**Datasets and Evaluation** To evaluate the performance of Wavelet Flow, we use several standard image datasets to directly compare against the reported results of previous methods. Specifically, we train and evaluate our model on natural image datasets at the commonly used resolutions and follow standard preprocessing: *ImageNet* [40] ( $32 \times 32$  and  $64 \times 64$ ) and *Large-scale Scene Understanding (LSUN) bedroom, tower, and church* outdoor [48] ( $64 \times 64$ ). We also train on two high resolution datasets at resolutions not previously reported: *CelebFaces Attributes High-Quality (CelebA-HQ)* [22] ( $1024 \times 1024$ ) and *Flickr-Faces-HQ (FFHQ)* [23] ( $1024 \times 1024$ ). We use the same CelebA-HQ dataset split used in [25]. FFHQ contains 70 000 high quality  $1024 \times 1024$  images of faces aligned and cropped from Flickr. This high resolution dataset has not been previously used in conjunction with normalizing flows. As no standard dataset split is available, we generate our own with 59 000, 4 000, and 7 000 images for training, validation and testing, respectively. Quantitative evaluations are based on average log likelihoods over a test set in the form of the commonly reported *bits per dimensions* (BPD) corresponding to intensity discretization into 256 bins. All experiments are performed with the original 8-bit images unless otherwise noted. Kingma and Dhariwal [25] reported that reducing the bit-depth of the data to 5-bit can improve the quality of samples; however, no such effect was observed with Wavelet Flow and consequently we use the original bit-depth of the data. For full details of the datasets, their experimental setup, and 5-bit quantitative results, see Appendix C and D.

**Results** Quantitative results in BPD are shown in Table 1. The Wavelet Flow models are competitive with other methods, outperforming Glow on ImageNet while somewhat underperforming Glow on LSUN but with significantly faster training. Training times for each dataset and scale vary with the smallest scales taking a few hours and largest scales typically requiring five or six days. The total

Model	ImageNet [40]		LSUN [48]			CelebA-HQ [22]	FFHQ [23]
	32 × 32	64 × 64	bedroom	tower	church		
			64 × 64			1024 × 1024	1024 × 1024
RealNVP [10]	4.28	3.98	2.72	2.81	3.08	-	-
Glow [25]	4.09	3.81	2.38	2.46	2.67	-	-
Wavelet Flow	4.08	3.78	2.41	2.49	2.74	1.34	2.07

Table 1: Quantitative performance in bits per dimension. RealNVP and Glow are not evaluated on CelebA-HQ 1024 or FFHQ 1024 as training is impractical at those resolutions.

training times for ImageNet at  $64 \times 64$  and CelebA-HQ at  $1024 \times 1024$  were 822 and 672 GPU hours, respectively. Exact training times for Glow [25] were not reported in the paper but are estimated<sup>2</sup> to be approximately 6,700 GPU hours to train on CelebA-HQ at  $256 \times 256$  and 3,700 GPU hours to train on LSUN bedroom at  $64 \times 64$ . In contrast, training Wavelet Flow on those datasets and resolutions take approximately 430 and 572 GPU hours, respectively,  $15\times$  and  $6\times$  faster than Glow. We also measure the average number of seconds-per-image over 100 iterations of training on our hardware. On CelebA-HQ at  $256 \times 256$ , ImageNet at  $64 \times 64$ , and LSUN at  $64 \times 64$ , we achieve speedups greater than  $30\times$  that of Glow, in terms of seconds-per-image. This is enabled, in part, because the smaller, simpler individual conditional models that make up Wavelet Flow allow for larger batch sizes than is possible with a single monolithic Glow model and their training can be more efficiently parallelized. More detailed training times can be found in Appendix D.

As described above, a Wavelet Flow can automatically be applied on lower resolution signals. To demonstrate this we use the model trained on ImageNet at  $64 \times 64$  and truncate it to evaluate at  $32 \times 32$ , getting a BPD of 4.16 vs. 4.08 with the model trained directly at  $32 \times 32$ . This difference is due to dequantization [17, 19]. Specifically, dequantization noise is low-pass filtered in the wavelet transform along with the original signal and is no longer uniform at lower resolutions and hence there are small (below a single pixel intensity increment) differences in the data distribution for the embedded lower resolution models. This was verified by using dequantization noise consistent with this low-pass filtered uniform noise during testing of the truncated model which achieves a BPD of 4.08, exactly the same as a Wavelet Flow trained directly on  $32 \times 32$  images. Note that this does not occur when modelling a truly continuous signal, where dequantization is not necessary. Further exploration of dequantization in Wavelet Flow remains a direction for future work.

To assess the qualitative performance of our model, we sampled from an annealed version of the estimated distribution using the MCMC approach described in Section 2.3. We explore a range of annealing parameters and find that only a small amount of annealing, *i.e.*,  $T = 0.97$ , is required to produce good visual results. In contrast, other methods typically require a large amount of annealing to produce plausible images, *e.g.*, Glow [25] reported results using  $T = 0.7$  for CelebA-HQ. Generated images for all datasets are shown in Fig. 2 and more are in Appendix E. Images generated at different values of  $T$  can be found in Fig. 3(a). Notably, at extremely low temperatures the images become somewhat blurry, likely indicating that the annealed distribution of detail coefficients (see below) has become too peaked at zero at finer scales. Further, lower values of  $T$  may cause problems with convergence of the MCMC based sampling approach.

High resolution samples from Wavelet Flow trained on CelebA-HQ and FFHQ at  $1024 \times 1024$  are shown in Figure 4 and more are in Appendix E. We also report a quantitative evaluation of Wavelet Flow on these datasets in Table 1 but note that comparison to other methods is not possible as training the baselines on high resolution imagery is impractical.

**Super Resolution** The conditional structure of a Wavelet Flow allows them to perform probabilistic super resolution by generating the detail coefficients given a lower resolution input image. That is, given an input image as  $\mathbf{I}_i$  we can generate  $\mathbf{D}_i$  by sampling from  $p(\mathbf{D}_i|\mathbf{I}_i)$  and construct  $\mathbf{I}_{i+1} = h^{-1}(\mathbf{I}_i, \mathbf{D}_i)$  to achieve a  $2\times$  increase in resolution. This process can be applied iteratively to recover higher resolutions. An example of  $8\times$  upsampling, from  $128 \times 128$  to  $1024 \times 1024$ , can be seen in Fig. 5. Note that our model is not trained specifically for super resolution, rather this is a notable byproduct of the scale conditional structure of Wavelet Flow. We present these results only as a demonstration and leave a full exploration of Wavelet Flow for super resolution as future work.

<sup>2</sup>Training times for Glow were estimated by inspecting the available training logs and along with additional details reported by the lead author here: <https://github.com/openai/glow/issues/37>



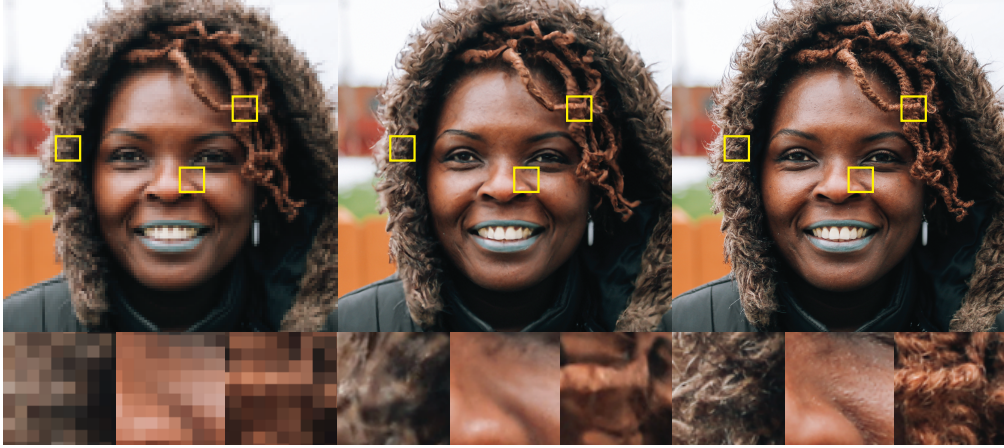


Figure 5: Wavelet Flow super resolution with  $T = 0.97$  trained on FFHQ from  $128 \times 128$  (left) to  $1024 \times 1024$  (middle) with ground truth (right) and magnified regions (bottom) for comparison.

**Effects of Annealing** Training with maximum likelihood (ML) typically results in models that favour diversity rather than specificity due to its “mean-seeking” tendency. Kingma and Dhariwal [25] further speculated that flow-based models over-estimate the entropy of the distribution. As a result, images directly drawn from ML trained models tend to be less realistic. Previous flow-based approaches (*e.g.*, [25, 33]) have instead shown samples drawn from an annealed version of the estimated distribution. We can see this over estimation of the entropy in the marginal distribution of the generated detail coefficients shown in Fig. 6. Specifically, without annealing the peak of the learned distribution of wavelet details is lower. However, after annealing, the distribution of detail coefficients matches well with the data, further supporting the choice of  $T = 0.97$ . In contrast, with the additive model we see that even with  $T = 0.4$  the distribution still does not match.

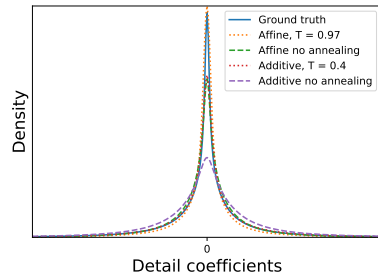


Figure 6: Marginal distributions of detail coefficients  $D_5$  for Wavelet Flow trained on CelebA-HQ.

**Additive vs. Affine Coupling** As discussed in Section 2.3, to draw samples from an annealed distribution in previous works (*e.g.*, [25, 33]), affine coupling layers are replaced with additive coupling layers to produce a model with a constant Jacobian determinant. While affine layers generally produce better quantitative results [10, 25], it is unknown whether they are also qualitatively better when annealed. Here, we present the first direct comparison between annealed additive and affine models. Fig. 3(b) and 3(c) compare samples from Wavelet Flows with additive and affine layers. Our results demonstrate that, in the case of Wavelet Flow, additive and affine layers have similar image quality. However, more aggressive annealing of the additive model is required. Further, as shown in Fig. 6, even with aggressive annealing, additive models still cannot match the marginal statistics of the detail coefficients as well as affine models. As a result we choose only to use a single, affine coupling-based model for both quantitative evaluation and sample generation.

**Evaluation of Sample Quality** Qualitatively Wavelet Flow appears to have somewhat worse performance than the Glow baseline. This is corroborated by FID scores [41] provided in Appendix D, but can also be seen in one specific aspect: spatially distant dependencies are not well captured by Wavelet Flow. In particular, global coherence of fine details, *e.g.*, eye colour, gaze direction, and hair texture, appear inconsistent over larger distances. This is most obvious when modelling human faces, and manifests as asymmetric eyes shown in Fig. 7, and inconsistent hair texture shown in Fig. 8. It is not immediately clear exactly how the wavelet decomposition, receptive field, patch based training, and conditioning, interact to cause this. Analysing the detail coefficients in Fig. 8 suggests that these inconsistencies mainly occur at higher frequencies.

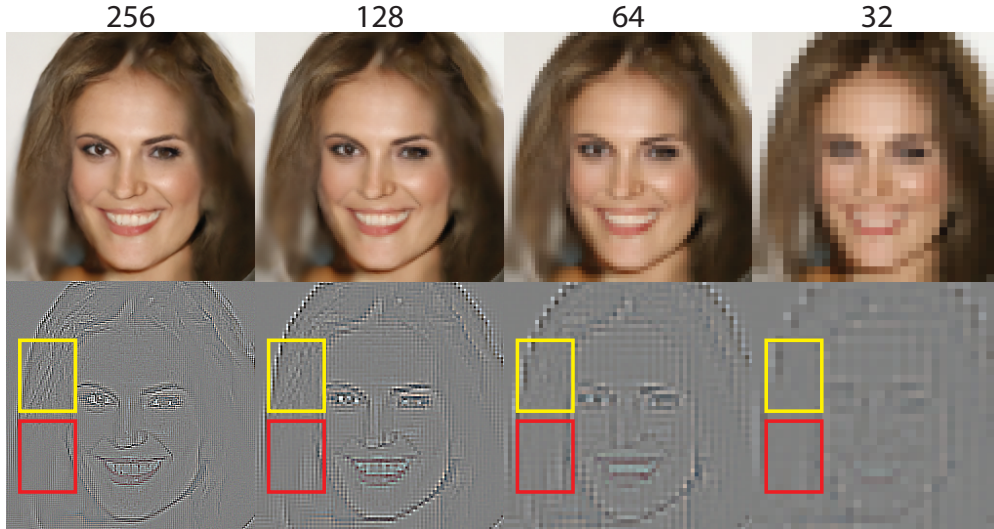


Figure 8: Texture inconsistency over large distances with Wavelet Flow. A sample from Wavelet Flow trained on CelebA-HQ at different scales (top), and visualizations of the corresponding detail coefficients (bottom). Two regions of interest are highlighted by yellow and red boxes. The yellow region has hair texture, while the red region is overly smooth. The corresponding regions in the detail coefficient visualizations show that the inconsistencies are mainly due to differences in the high frequencies details.

#### 4 Discussion and Future Work

In this paper, we introduced Wavelet Flow, a multi-scale, conditional normalizing flow architecture based on wavelets. We showed that the resulting model is up to  $15\times$  faster to train and enables the training of generative models for high resolution data which is impractical with previous flow-based approaches. We also showed how the multi-scale structure of our Wavelet Flow model could be used to extract consistent distributions of low resolution signals, as well as to perform super resolution.

There remains several promising directions for future work. The choice of wavelet was not considered here; a Haar wavelet was used for simplicity. Numerous wavelets exist [35] and it is unclear how the choice of wavelet may impact performance. This paper focused on natural images, but Wavelet Flow is directly applicable to other domains, *e.g.*, video, medical imaging, and audio. With images there remains work to explore the use of Wavelet Flow for problems such as image restoration and super resolution. While we explored some architecture choices for the conditional flows, we expect that improvements in performance will be found with other architectures, *e.g.*, [17, 33, 13, 20]. Initial experiments investigating the reduced global coherence in Wavelet Flow were inconclusive; however, we suspect that further architecture search may help address these issues. Further, as noted in Sec. 3, dequantization in a Wavelet Flow can interfere with certain desirable multi-scale properties. Adapting dequantization for use in a Wavelet Flow may rectify this and is likely to improve performance as it has with other normalizing flow models [17, 19].



Figure 7: Detail inconsistency over large distances with Wavelet Flow. A sample from Wavelet Flow trained on CelebA-HQ at different resolutions enlarged around the asymmetrically coloured eyes. The asymmetry only becomes apparent at higher resolutions.



## Acknowledgments and Disclosure of Funding

This work was started as part of J.J.Y.’s internship at Borealis AI and was supported by the Mitacs Accelerate Program, funded in part by the Canada First Research Excellence Fund (CFREF) for the Vision: Science to Applications (VISTA) program (M.A.B.) and the NSERC Discovery Grant program (M.A.B., K.G.D.). K.G.D. contributed to this work in his capacity as an Associate Professor at Ryerson University.

## Broader Impact

This work contributes to the domain of generative image modelling, which constructs probabilistic models of images, allowing the generation, and manipulation of high resolution images. As this domain grows, these tasks become more accessible due to reduced labour, and skill barriers. On a positive side, this accessibility can empower artists and content creators with powerful tools for their craft. Many other processes used today are data driven, *e.g.*, semantic segmentation, and could benefit from the ability to create new data. Generative models are also useful in applications beyond content generation. In particular, they can be used as priors in other signal processing tasks including image restoration, and super resolution. The computational costs of machine learning are of increasing concern as a potential future source of social and economic inequality. Reducing the need for specialized, large-scale hardware for training, as the approach proposed here does, can lower the barrier to entry for individuals and groups which would otherwise be unable to afford the large compute clusters necessary.

As with all tools, generative models have no intentions of their own. Their impact is defined by those who wield them. Media platforms play an important role in our lives, and as a result can be used for disinformation. A major difficulty in preventing disinformation is the asymmetry between the capacity to create and detect disinformation. If the detection of disinformation is more difficult than its creation, its prevention may become impossible in practice. Our contributions primarily serve to reduce the costs of content generation. Specifically, the ability to operate on high resolution images at a reduced cost makes it easier for actors that wish to create convincing content in large volumes. Consequently, this could worsen the battle against disinformation.

Even without actors that are intentionally malicious, reduced barriers to these tools could increase the absolute amount of unintentional misuse. The nature of generative models encourages them to adopt biases in the data used to train them. Without caution, a user could introduce biases to a generative model that may discriminate against certain groups of people. This model could then be easily used to create large quantities of data that contain this bias. This could take the form of data used in other downstream processes, or directly as content consumed by people.

These concerns assume unopposed misuse of generative methods. Complementary research into the detection of generated content could mitigate these potential consequences. Much like how active research into adversarial attacks continuously competes with research into robust recognition methods, generative methods can exist at an equilibrium with methods used to detect their use, and biases, preventing runaway consequences.

## References

- [1] C. H. Anderson. A filter-subtract-decimate hierarchical pyramid signal analyzing and synthesizing technique, 1987. US Patent 4,718,104, Washington, DC.
- [2] Lynton Ardizzone, Carsten Lüth, Jakob Kruse, Carsten Rother, and Ullrich Köthe. Guided image generation with conditional invertible neural networks. *arXiv preprint arXiv:1907.02392*, 2019.
- [3] Ronald Newbold Bracewell. *The Fourier transform and its applications*. McGraw-Hill New York, 1986. ISBN 9780070070134.
- [4] Joan Bruna and Stéphane Mallat. Invariant scattering convolution networks. *IEEE Transactions on Pattern Analysis and Machine Intelligence (PAMI)*, 35(8):1872–1886, 2013.
- [5] P. Burt and E. Adelson. The Laplacian pyramid as a compact image code. *IEEE Transactions on Communications*, 31(4):532–540, 1983.

- [6] Peter J. Burt. Fast filter transform for image processing. *Computer Graphics and Image Processing*, 16(1):20 – 51, 1981.
- [7] James L. Crowley and Alice C. Parker. A representation for shape based on peaks and ridges in the difference of low-pass transform. *IEEE Transactions on Pattern Analysis and Machine Intelligence (PAMI)*, 6(2):156–170, 1984.
- [8] Emily L. Denton, Soumith Chintala, Arthur Szlam, and Rob Fergus. Deep generative image models using a Laplacian pyramid of adversarial networks. In *Neural Information Processing Systems (NeurIPS)*, pages 1486–1494, 2015.
- [9] Laurent Dinh, David Krueger, and Yoshua Bengio. NICE: Non-linear independent components estimation. In *Proceedings of the International Conference on Learning Representations (ICLR) Workshop*, 2015.
- [10] Laurent Dinh, Jascha Sohl-Dickstein, and Samy Bengio. Density estimation using RealNVP. In *Proceedings of the International Conference on Learning Representations (ICLR)*, 2017.
- [11] Garoe Dorta, Sara Vicente, Lourdes Agapito, Neill D.F. Campbell, Simon Prince, and Ivor Simpson. Laplacian pyramid of conditional variational autoencoders. In *Proceedings of the European Conference on Visual Media Production (CVMP)*, pages 1–9, 2017.
- [12] Ian J. Goodfellow, Jean Pouget-Abadie, Mehdi Mirza, Bing Xu, David Warde-Farley, Sherjil Ozair, Aaron C. Courville, and Yoshua Bengio. Generative adversarial nets. In *Neural Information Processing Systems (NeurIPS)*, 2014.
- [13] Will Grathwohl, Ricky T. Q. Chen, Jesse Bettencourt, Ilya Sutskever, and David Duvenaud. FFIORD: Free-form continuous dynamics for scalable reversible generative models. In *Proceedings of the International Conference on Learning Representations (ICLR)*, 2019.
- [14] Ishaan Gulrajani, Kundan Kumar, Faruk Ahmed, Adrien Ali Taiga, Francesco Visin, David Vazquez, and Aaron Courville. PixelVAE: A latent variable model for natural images. In *Proceedings of the International Conference on Learning Representations (ICLR)*, 2017.
- [15] Alfred Haar. Zur Theorie der orthogonalen Funktionensysteme. *Mathematische Annalen*, 69(3): 331–371, 1910.
- [16] Kaiming He, Xiangyu Zhang, Shaoqing Ren, and Jian Sun. Deep residual learning for image recognition. In *Proceedings of the IEEE Conference on Computer Vision and Pattern Recognition (CVPR)*, 2016.
- [17] Jonathan Ho, Xi Chen, Aravind Srinivas, Yan Duan, and Pieter Abbeel. Flow++: Improving flow-based generative models with variational dequantization and architecture design. In *Proceedings of the International Conference on Machine Learning (ICML)*, 2019.
- [18] Matthew D Hoffman and Andrew Gelman. The no-u-turn sampler: Adaptively setting path lengths in Hamiltonian Monte Carlo. *Journal of Machine Learning Research*, 15(1):1593–1623, 2014.
- [19] Emiel Hoogeboom, Taco S. Cohen, and Jakub M. Tomczak. Learning discrete distributions by dequantization. *arXiv preprint, arXiv:2001.11235*, 2020.
- [20] Priyank Jaini, Kira A. Selby, and Yaoliang Yu. Sum-of-squares polynomial flow. In *Proceedings of the International Conference on Machine Learning (ICML)*, 5 2019.
- [21] Animesh Karnewar, Oliver Wang, and Raghu Sesha Iyengar. MSG-GAN: Multi-scale gradient GAN for stable image synthesis. *CoRR*, abs/1903.06048, 2019.
- [22] Tero Karras, Timo Aila, Samuli Laine, and Jaakko Lehtinen. Progressive growing of GANs for improved quality, stability, and variation. In *Proceedings of the International Conference on Learning Representations (ICLR)*, 2018.
- [23] Tero Karras, Samuli Laine, and Timo Aila. A style-based generator architecture for generative adversarial networks. In *Proceedings of the IEEE Conference on Computer Vision and Pattern Recognition (CVPR)*, pages 4401–4410, 2019.
- [24] Diederik P. Kingma and Jimmy Ba. Adam: A method for stochastic optimization. In *Proceedings of the International Conference on Learning Representations (ICLR)*, 2014.
- [25] Diederik P. Kingma and Prafulla Dhariwal. Glow: Generative flow with invertible 1x1 convolutions. In *Neural Information Processing Systems (NeurIPS)*, pages 10215–10224, 2018.

- [26] Diederik P. Kingma and Max Welling. An introduction to variational autoencoders. *arXiv preprint, arXiv:1906.02691*, 2019.
- [27] Ivan Kobyzev, Simon Prince, and Marcus Brubaker. Normalizing flows: An introduction and review of current methods. *IEEE Transactions on Pattern Analysis and Machine Intelligence (PAMI)*, 2020.
- [28] Jan J. Koenderink. The structure of images. *Biological Cybernetics*, 50(5):363–370, 1984.
- [29] Junpeng Lao, Christopher Suter, Ian Langmore, Cyril Chimisov, Ashish Saxena, Pavel Sountsov, Dave Moore, Rif A. Saurous, Matthew D. Hoffman, and Joshua V. Dillon. tfp.mcmc: Modern Markov chain Monte Carlo tools built for modern hardware. *arXiv preprint, arXiv:2002.01184*, 2020.
- [30] Tony Lindeberg. Scale-space for discrete signals. *IEEE Transactions on Pattern Analysis and Machine Intelligence (PAMI)*, 12(3):234–254, 1990.
- [31] Tony Lindeberg. Scale-space theory: A basic tool for analyzing structures at different scales. *Journal of Applied Statistics*, 21(1-2):225–270, 1994.
- [32] Ziwei Liu, Ping Luo, Xiaogang Wang, and Xiaoou Tang. Deep learning face attributes in the wild. In *Proceedings of International Conference on Computer Vision (ICCV)*, 2015.
- [33] Xuezhe Ma, Xiang Kong, Shanghang Zhang, and Eduard Hovy. MaCow: Masked convolutional generative flow. In *Neural Information Processing Systems (NeurIPS)*, pages 5891–5900, 2019.
- [34] Stéphane Mallat. A theory for multiresolution signal decomposition: The wavelet representation. *IEEE Transactions on Pattern Analysis and Machine Intelligence (PAMI)*, 11(7):674–693, 1989.
- [35] Stephane Mallat. *A wavelet tour of signal processing: The Sparse Way*. Elsevier, 3rd edition, 2009. ISBN 9780123743701.
- [36] David Marr. *Vision: A Computational Investigation into the Human Representation and Processing of Visual Information*. Henry Holt and Co., Inc., USA, 1982. ISBN 0716715678.
- [37] George Papamakarios, Eric Nalisnick, Danilo Jimenez Rezende, Shakir Mohamed, and Balaji Lakshminarayanan. Normalizing flows for probabilistic modeling and inference. *arXiv preprint, arXiv:1912.02762*, 2019.
- [38] Ali Razavi, Aäron van den Oord, and Oriol Vinyals. Generating diverse high-fidelity images with VQ-VAE-2. In *Neural Information Processing Systems (NeurIPS)*, pages 14837–14847, 2019.
- [39] Scott E. Reed, Aäron van den Oord, Nal Kalchbrenner, Sergio Gomez Colmenarejo, Ziyu Wang, Yutian Chen, Dan Belov, and Nando de Freitas. Parallel multiscale autoregressive density estimation. In *Proceedings of the International Conference on Machine Learning (ICML)*, pages 2912–2921, 2017.
- [40] Olga Russakovsky, Jia Deng, Hao Su, Jonathan Krause, Sanjeev Satheesh, Sean Ma, Zhiheng Huang, Andrej Karpathy, Aditya Khosla, Michael Bernstein, Alexander C. Berg, and Li Fei-Fei. ImageNet large scale visual recognition challenge. *International Journal of Computer Vision (IJCV)*, 115(3):211–252, 2015.
- [41] Tim Salimans, Ian J. Goodfellow, Wojciech Zaremba, Vicki Cheung, Alec Radford, and Xi Chen. Improved techniques for training GANs. In *Neural Information Processing Systems (NeurIPS)*, 2016.
- [42] Tim Salimans, Andrej Karpathy, Xi Chen, and Diederik P. Kingma. PixelCNN++: Improving the PixelCNN with discretized logistic mixture likelihood and other modifications. In *Proceedings of the International Conference on Learning Representations (ICLR)*, 2017.
- [43] Tamar Rott Shaham, Tali Dekel, and Tomer Michaeli. SinGAN: Learning a generative model from a single natural image. In *Proceedings of the International Conference on Computer Vision (ICCV)*, pages 4569–4579, 2019.
- [44] Aaron van den Oord, Nal Kalchbrenner, and Koray Kavukcuoglu. Pixel recurrent neural networks. In *Proceedings of the International Conference on Machine Learning (ICML)*, 2016.
- [45] Ting-Chun Wang, Ming-Yu Liu, Jun-Yan Zhu, Andrew Tao, Jan Kautz, and Bryan Catanzaro. High-resolution image synthesis and semantic manipulation with conditional GANs. In *Proceedings of the IEEE Conference on Computer Vision and Pattern Recognition (CVPR)*, pages 8798–8807, 2018.

- [46] Christina Winkler, Daniel Worrall, Emiel Hoogeboom, and Max Welling. Learning likelihoods with conditional normalizing flows. *arXiv preprint arXiv:1912.00042*, 2019.
- [47] Andrew P. Witkin. Scale-space filtering. In *Proceedings of the International Joint Conference on Artificial Intelligence (IJCAI)*, pages 1019–1022, 1983.
- [48] Fisher Yu, Ari Seff, Yinda Zhang, Shuran Song, Thomas Funkhouser, and Jianxiong Xiao. LSUN: Construction of a large-scale image dataset using deep learning with humans in the loop. *arXiv preprint arXiv:1506.03365*, 2015.
- [49] Han Zhang, Tao Xu, and Hongsheng Li. StackGAN: Text to photo-realistic image synthesis with stacked generative adversarial networks. In *Proceedings of the International Conference on Computer Vision (ICCV)*, pages 5908–5916, 2017.
- [50] Han Zhang, Tao Xu, Hongsheng Li, Shaoqing Zhang, Xiaoqiang Wang, Xiaoqi Huang, and Dimitris N. Metaxas. StackGAN++: Realistic image synthesis with stacked generative adversarial networks. *IEEE Transactions on Pattern Analysis and Machine Intelligence (PAMI)*, 41(8): 1947–1962, 2019.

## A Supplementary code

Code and project page is available at: <https://yorkucvil.github.io/Wavelet-Flow>

## B MCMC Sampling with Wavelet Flow

As discussed in Sec. 2.3, MCMC (*i.e.*, No-U-Turn Sampler (NUTS) algorithm [18, 29]) is used to draw annealed samples from the annealed Wavelet Flow model. In this section, we describe the annealed sampling process. First, we describe how MCMC can be used to draw samples from any distribution constructed as a normalizing flow. Next, we describe how the Wavelet Flow structure in particular is used to enable faster sampling.

### B.1 MCMC on an Annealed Flow

The target distribution for MCMC is the annealed normalizing flow and can be written as:

$$\pi_{\mathbf{x}}(\mathbf{x}) \propto p_{\mathbf{x}}(\mathbf{x})^\gamma \quad (7)$$

$$= p_{\mathbf{z}}(\mathbf{f}(\mathbf{x}))^\gamma |\det \mathbf{J}(\mathbf{x})|^\gamma, \quad (8)$$

where  $\gamma = 1/T^2$  is the annealing parameter,  $\mathbf{f}$  is the normalizing flow transformation,  $\mathbf{J}$  is the Jacobian of  $\mathbf{f}$ , and the degree of annealing is specified as a *temperature* with  $T = 1/\sqrt{\gamma}$ , following the convention of [25].

The No-U-Turn Sampler (NUTS) [18] requires only that the unnormalized probability density and its gradients can be evaluated and can be applied directly to  $\pi_{\mathbf{x}}(\mathbf{x})$ ; however, the complex dependencies that exist between dimensions of  $\mathbf{x}$  can produce a challenging geometry of the probability density which can be difficult for MCMC algorithms to sample from efficiently. Since we know the form of the density is closely related to a known normalizing flow, we can use the inverse of this flow,  $\mathbf{g}$ , to reparameterize the density such that it becomes exactly Gaussian (and hence easier to sample) when  $\gamma = 1$ . For  $\gamma \neq 1$  the geometry should still be close to Gaussian and hence easier to sample from, particularly with values of  $\gamma$  close to 1. Reparameterizing the annealed distribution in terms of  $\mathbf{z}$  gives:

$$\pi_{\mathbf{z}}(\mathbf{z}) \propto \pi_{\mathbf{x}}(\mathbf{g}(\mathbf{z})) |\det \mathbf{H}(\mathbf{z})| \quad (9)$$

$$= p_{\mathbf{z}}(\mathbf{f}(\mathbf{g}(\mathbf{z})))^\gamma |\det \mathbf{J}(\mathbf{g}(\mathbf{z}))|^\gamma |\det \mathbf{H}(\mathbf{z})| \quad (10)$$

$$= p_{\mathbf{z}}(\mathbf{z})^\gamma |\det \mathbf{H}(\mathbf{z})|^{1-\gamma}, \quad (11)$$

where  $\mathbf{H} = \frac{\partial \mathbf{g}}{\partial \mathbf{z}}$  is the Jacobian of  $\mathbf{g}$ , and the last line follows because  $\mathbf{g}$  is the inverse of the flow transformation  $\mathbf{f}$ , *i.e.*,  $\mathbf{g} = \mathbf{f}^{-1}$ , and hence their Jacobians (and their determinants) are also inverses of each other. NUTS is then used to perform MCMC on  $\pi_{\mathbf{z}}(\mathbf{z})$ . Samples from this Markov chain can then be transformed into samples from  $\pi_{\mathbf{x}}(\mathbf{x})$  by computing  $\mathbf{g}(\mathbf{z})$  like in a normalizing flow. In practice, we found that sampling in terms of  $\mathbf{z}$  using the NUTS algorithm [18] is more efficient and can be done with a larger step size and fewer divergences, compared to sampling in terms of  $\mathbf{x}$ . We use the implementation of NUTS provided in [29].

### B.2 Multi-scale MCMC with Wavelet Flow

The above procedure can be inefficient if applied to the entire distribution of wavelet coefficients due to the high dimensionality and complexity of the distributions. Instead, it is applied levelwise. In particular, first samples are drawn using MCMC as described above from  $p(\mathbf{I}_0)^\gamma$ , then using the last sample from that chain we sample from  $p(\mathbf{D}_0|\mathbf{I}_0)^\gamma$ , construct  $\mathbf{I}_1 = h^{-1}(\mathbf{I}_0, \mathbf{D}_0)$  and continue this

procedure for  $\mathbf{D}_1$ ,  $\mathbf{D}_2$  and so on until all detail coefficients have been generated and a sample of  $\mathbf{I}$  is drawn from the annealed distribution. This algorithm is shown in Algorithm 1.

---

**Algorithm 1:** Annealed sampling from Wavelet Flow using NUTS.  $\gamma$  is the annealing parameter,  $N$  is the number of levels in the Wavelet Flow, and  $m$  is the minimum number of NUTS steps. In our experiments,  $m$  is set to 30.  $\mathbf{z}_i$  is the base value of the flow  $\mathbf{g}_i$  used to produce  $\mathbf{D}_i$ . Subscript  $b$  indicates components for the initial base image.

---

```

Given  $\gamma, N, m$ :
Sample  $\hat{\mathbf{z}}_b \sim p_{\mathbf{Z}_b}^\gamma(\mathbf{z}_b)$ 
Sample  $\mathbf{z}_b \sim \pi_{\mathbf{Z}_n}(\mathbf{z}_b)$  using NUTS, initialized with  $\hat{\mathbf{z}}_b$ , and  $m$  steps
Set  $\mathbf{I}_0 \leftarrow \mathbf{g}_b(\mathbf{z}_b)$ 
for  $i \leftarrow 0$  to  $N - 1$  do
    Sample  $\hat{\mathbf{z}}_i \sim p_{\mathbf{Z}_i}^\gamma(\mathbf{z}_i)$ 
    Sample  $\mathbf{z}_i \sim \pi_{\mathbf{Z}_i}(\mathbf{z}_i | \mathbf{I}_i)$  using NUTS, initialized with  $\hat{\mathbf{z}}_i$ , and  $m$  steps
    Set  $\mathbf{D}_i \leftarrow \mathbf{g}_i(\mathbf{z}_i | \mathbf{I}_i)$ 
    Set  $\mathbf{I}_{i+1} \leftarrow h^{-1}(\mathbf{I}_i, \mathbf{D}_i)$ 
end

```

---

In our experiments, the Markov chains are initialized with a sample from  $p_{\mathbf{Z}}(\mathbf{f}(\mathbf{g}(\mathbf{z})))^\gamma$ , which is straightforward since it is an annealed Gaussian and annealing simply scales the standard deviation. This provides a reasonable initialization which is exact in the case where the flow has a constant volume correction term or  $\gamma = 1$ . Samples from this initialization are not proper samples from the annealed distribution but can still look reasonable, further suggesting that it is a good initialization. Dual averaging adaptation is used to adjust the step size for the first 10 steps of NUTS [18]. A minimum of 30 steps are taken before the next accepted proposal is taken as the sample. These hyper-parameters were chosen since they gave good qualitative performance without using too much compute. In our experiments, we observed that it takes roughly 30 minutes to sample an annealed image at  $256 \times 256$  using  $T = 0.97$  on CelebA-HQ. It roughly takes an additional 50 minutes and 35 hours to further reach resolutions of  $512 \times 512$  and  $1024 \times 1024$ , respectively. Levelwise sampling can exploit parallelism at coarser scales but GPU memory limits when sampling details at higher resolutions. The time it takes to draw samples using NUTS also is dependent on  $T$  with values of  $T$  further from 1 generally taking longer. This is as expected as the target posterior for MCMC is exactly an isotropic Gaussian for  $T = 1$  and becomes less Gaussian-like as  $T$  varies from 1.

## C Datasets and experimental setup

The details about the datasets used are outlined below.

**ImageNet [40]** Two downsampled versions at resolutions of  $32 \times 32$  and  $64 \times 64$  are used. The training set consists of 1.28 million images, and the validation set contains 50 000 images. The validation set is used as the test set, which is also done in [10, 25].

**LSUN [48]** This dataset contains multiple categories, but experiments are only performed on *bedroom*, *tower*, and *church* which are most commonly used in generative modelling papers. The training sets of bedroom, tower, and church, contain three million, 700 000, and 126 000 images, respectively. The validation sets of all three categories contain 300 images each. Image dimensions in LSUN are not constant, pre-processing steps from [10] are performed to downsample the smallest side to 96 pixels before taking  $64 \times 64$  random crops. The validation set is used as the test set.

**CelebA-HQ [22]** This dataset is an extension of the original CelebFaces Attributes dataset [32] which contains  $1024 \times 1024$  images produced by applying inpainting and super resolution to aligned and cropped images. The 30 000 images in the dataset are separated into a training and test set using the same split as in [25]. The lower levels of the Wavelet Flow experienced overfitting, so a validation set is used to perform early stopping. The train, validation, and test sets contain 26 000, 1 000, and 3 000 images, respectively.

**FFHQ [23]** contains 70 000 high quality  $1024 \times 1024$  aligned and cropped face images retrieved from Flickr. A training, validation, and test split were generated with 59 000, 4 000, and 7 000 images, respectively. As with CelebA-HQ lower levels of Wavelet Flow experienced overfitting and early stopping is used.

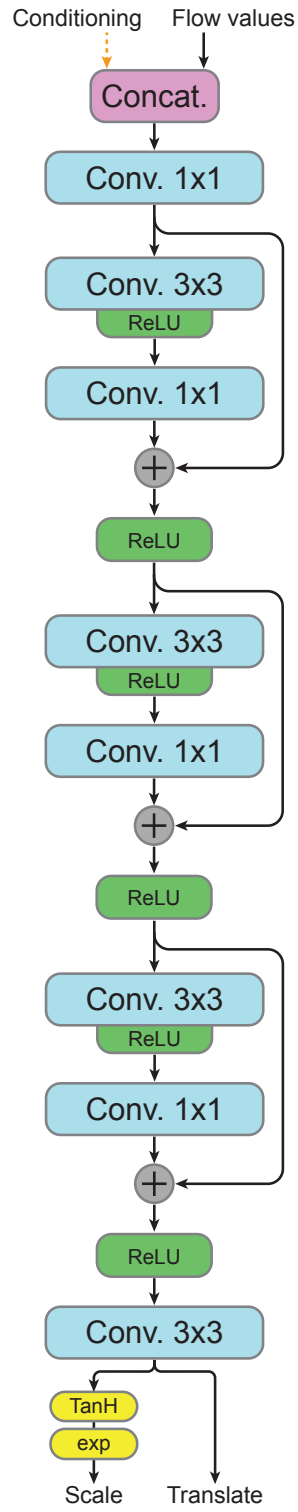


Figure 9: Coupling network architecture.



Model/ Hyper-params.	Resolution										
	1	2	4	8	16	32	64	128	256	512	1024
<b>ImageNet [40] 32</b>											
# Flow steps	8	8	16	16	16	16	-	-	-	-	-
Conv. channels	128	128	128	128	128	256	-	-	-	-	-
Patch size	1	2	4	8	16	16	-	-	-	-	-
Batch size	64	64	64	64	64	64	-	-	-	-	-
Parameter count	4m	4m	8m	8m	8m	32m	-	-	-	-	-
<b>ImageNet [40] 64</b>											
# Flow steps	8	8	16	16	16	16	16	-	-	-	-
Conv. channels	128	128	128	128	128	256	256	-	-	-	-
Patch size	1	2	4	8	16	16	32	-	-	-	-
Batch size	64	64	64	64	64	64	48	-	-	-	-
Parameter count	4m	4m	8m	8m	8m	32m	32m	-	-	-	-
<b>LSUN [48] (bedroom/tower /church) 64</b>											
# Flow steps	8	8	16	16	16	16	30	-	-	-	-
Conv. channels	16	64	64	64	64	128	320	-	-	-	-
Patch size	1	2	4	8	16	32	64	-	-	-	-
Batch size	64	64	64	64	64	64	64	-	-	-	-
Parameter count	68k	1m	2m	2m	2m	8m	93m	-	-	-	-
<b>CelebA-HQ [22]/ FFHQ [23] 1024</b>											
# Flow steps	8	8	16	16	16	16	16	16	16	16	16
Conv. channels	64	64	64	128	128	128	128	128	128	128	128
Patch size	1	2	4	8	16	32	32	64	64	64	64
Batch size	64	64	64	64	64	64	64	64	64	64	64
Parameter count	1m	1m	2m	8m	8m	8m	8m	8m	8m	8m	8m

Table 2: Hyper-parameters used with Wavelet Flow per level, and across the evaluation datasets.

As stated in Sec. 3 of the manuscript, hyper-parameters are set differently for each dataset to keep the number of parameters below but within the range of compared methods. These hyper-parameters are shown in Table 2. The number of parameters for each variant is show in Table 3.

Model	ImageNet [40]		LSUN [48]	CelebA-HQ [22] & FFHQ [23]
	32 × 32	64 × 64	64 × 64	1024 × 1024
RealNVP [10]	46m	96m	96m	-
Glow [25]	66m	111m	111m	-
Wavelet Flow	64m	96m	108m	70m

Table 3: Comparison of the total number of parameters used in Wavelet Flow, Glow, and RealNVP.

Coupling networks use a residual architecture [16], shown in Fig. 9. Inputs used to condition a coupling layer are concatenated to the input of its coupling network. As in [10], a *hyperbolic tangent* is applied to the scale component of the affine transform. The number of output channels in the convolutional layers is the same across the entire level of a Wavelet Flow.

Coupling layers are arranged into *steps*. Following Glow [25], the forward pass of a step is composed of an *activation normalization* (actnorm), *invertible*  $1 \times 1$ , and a coupling layer.

The Haar transformation used is shown in Fig. 10. The values of the low-pass component is effectively two times the box-downsampled image. In practice, it may be convenient to scale the low-pass component by  $\frac{1}{2}$  to eliminate any inconvenient scaling factors.

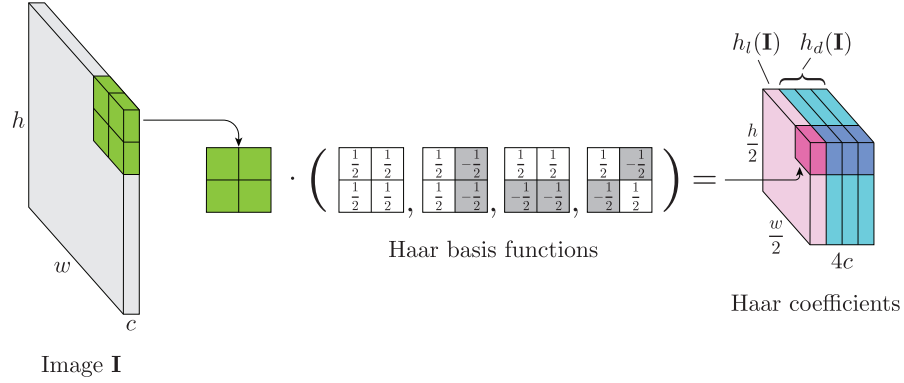


Figure 10: A Haar transformation on a single channel image. In practice, the Haar transformation is applied channel-wise. This transformation produces a low-pass and detail component denoted as  $h_l$  and  $h_d$ , respectively.  $h_d$  is comprised of the coefficients generated by the last three Haar filters that resemble vertical, horizontal, and diagonal derivative filters.

## D Additional results

Table 4 provides wall-clock times for training Wavelet Flow on each dataset, and at each level. Times also consider early stopping, where applicable.

Timing measured in seconds-per-image is provided in Table 5. Results are averaged over 100 iterations.

Additional quantitative results in bits-per-dimension for 5-bit CelebA-HQ at  $256 \times 256$  is shown in Table 6.

Frechet Inception Distance [41] scores for Glow and Wavelet flow on LSUN  $64 \times 64$  are shown in Table 7.

Level	Resolution	FFHQ [23]	CelebA-HQ [22]	ImageNet [40]	LSUN [48]
0	$1 \times 1$	6	6	6	6
1	$2 \times 2$	6	6	96	12
2	$4 \times 4$	6	6	48	14
3	$8 \times 8$	6	6	168	36
4	$16 \times 16$	18	12	168	48
5	$32 \times 32$	120	36	168	120
6	$64 \times 64$	120	120	168	336
7	$128 \times 128$	120	120	-	-
8	$256 \times 256$	120	120	-	-
9	$512 \times 512$	156	120	-	-
10	$1024 \times 1024$	168	120	-	-
Total		846	672	822	572

Table 4: Wavelet Flow training times in GPU hours on the evaluation datasets.

Method	CelebA-HQ [22] $256 \times 256$	ImageNet [40] $64 \times 64$	LSUN [48] $64 \times 64$
Glow [25]	1.79	0.956	0.954
Ours	0.0147	0.0144	0.0293

Table 5: Training speed measured using seconds-per-image averaged over 100 iterations. Values for Glow were obtained by running their provided code on our hardware, a single NVIDIA TITAN X (Pascal) GPU, and without using any distributed computation frameworks. Note that the Wavelet Flow model for CelebA-HQ  $256 \times 256$  is contained within the larger model for  $1024 \times 1024$  images.

Method	CelebA-HQ [22] $256 \times 256$ 5-bit
Glow [25] (Additive)	1.03
Ours (Additive)	1.12
Ours (Affine)	0.94

Table 6: Quantitative results in bits-per-dimension on 5-bit CelebA-HQ  $256 \times 256$ .

Method	LSUN [48] $64 \times 64$		
	Bedrooms	Tower	Church
Glow [25] (affine)	60.03	54.17	59.35
Ours	121.20	87.20	93.08

Table 7: Frechet Inception Distance [41] scores on LSUN  $64 \times 64$  between Glow (affine) and Wavelet Flow, both without annealing.

## E Additional samples

Additional samples without annealing are shown in Figs. 11, 12, 13, 14, 15, 16, 17. Additional samples with annealing using the previously described MCMC method with  $T = 0.97$ , are shown in Figs. 18, 19, 20, 21, 22, 23, 24. Additional high resolution samples from CelebA-HQ, and FFHQ, are shown in Figs. 25, 26. Additional  $8\times$  super resolution samples from CelebA-HQ, and FFHQ, are shown in Figs. 27, 28. Note that these samples are stored in this manuscript using JPEG compression to meet file size limits on arXiv. Please visit <https://yorkucvil.github.io/Wavelet-Flow> for the same figures in PNG format.



Figure 11: Samples from ImageNet ( $32 \times 32$ ) without annealing.



Figure 12: Samples from ImageNet ( $64 \times 64$ ) without annealing.





Figure 13: Samples from LSUN bedroom ( $64 \times 64$ ) without annealing.

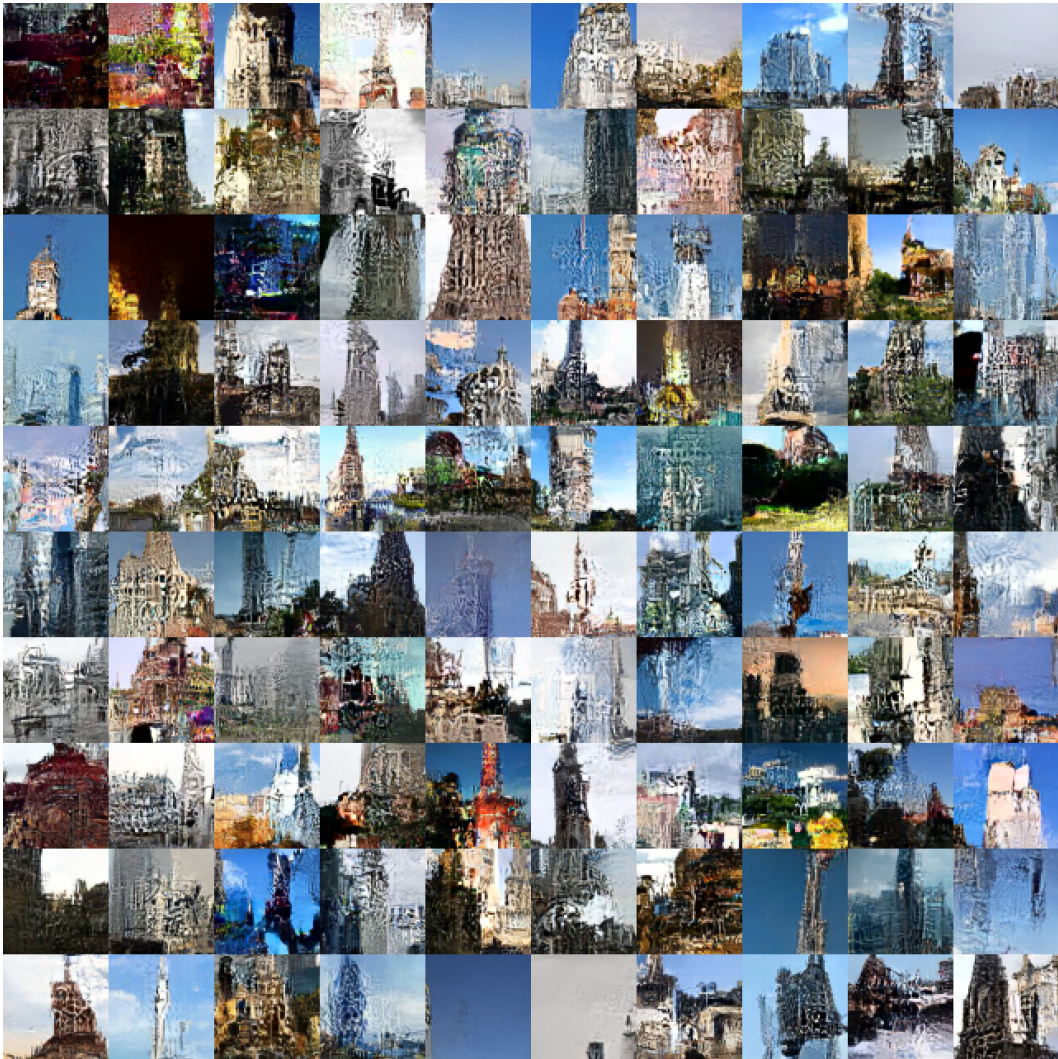


Figure 14: Samples from LSUN tower ( $64 \times 64$ ) without annealing.





Figure 15: Samples from LSUN church ( $64 \times 64$ ) without annealing.





Figure 16: Samples from CelebA-HQ ( $256 \times 256$ ) without annealing.





Figure 17: Samples from FFHQ ( $256 \times 256$ ) without annealing.



Figure 18: Annealed samples from ImageNet ( $32 \times 32$ ), with  $T = 0.97$ .



Figure 19: Annealed samples from ImageNet ( $64 \times 64$ ), with  $T = 0.97$ .





Figure 20: Annealed samples from LSUN bedroom ( $64 \times 64$ ), with  $T = 0.97$ .

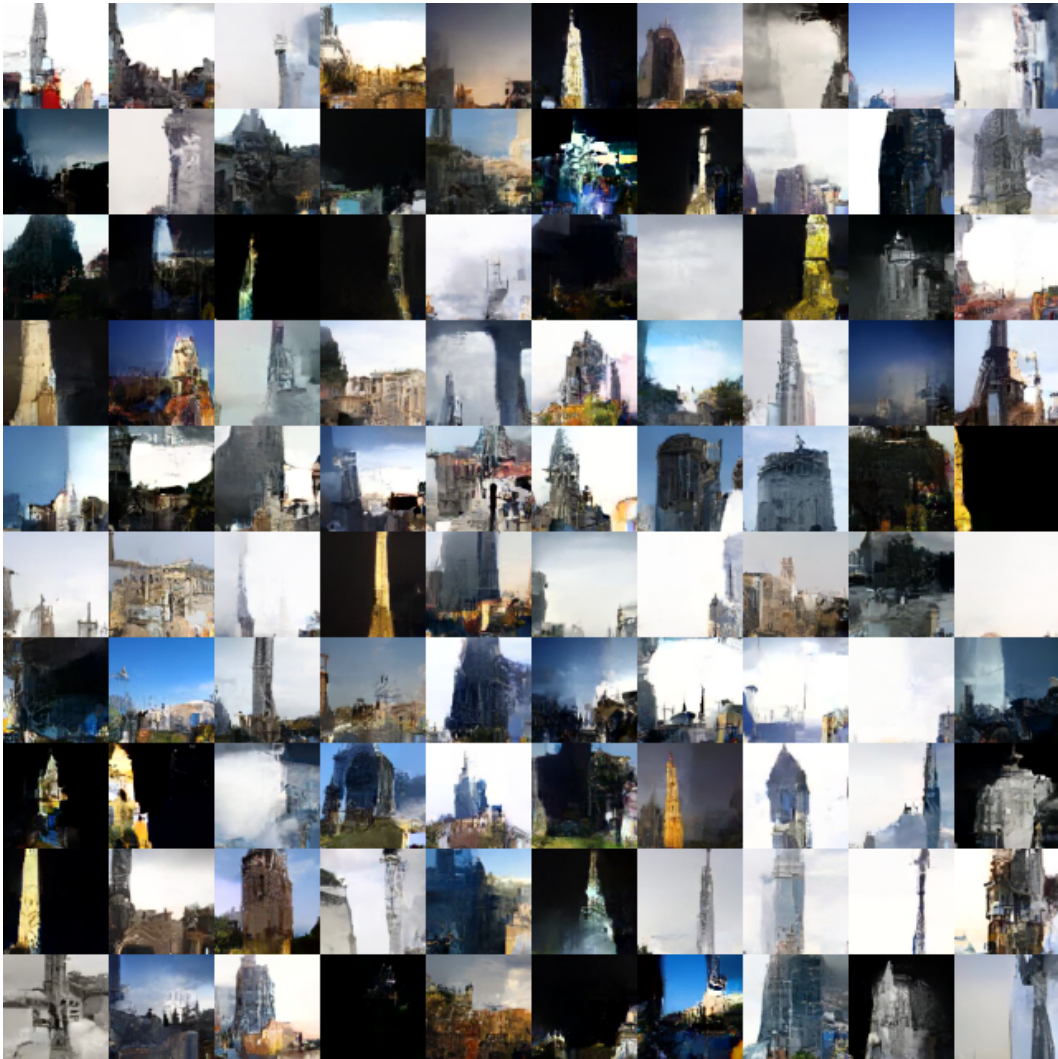


Figure 21: Annealed samples from LSUN tower ( $64 \times 64$ ), with  $T = 0.97$ .





Figure 22: Annealed samples from LSUN church ( $64 \times 64$ ), with  $T = 0.97$ .



Figure 23: Annealed samples from CelebA-HQ ( $256 \times 256$ ), with  $T = 0.97$ .





Figure 24: Annealed samples from FFHQ ( $256 \times 256$ ), with  $T = 0.97$ .



Figure 25: Annealed high resolution ( $1024 \times 1024$ ) samples from CelebA-HQ, with  $T = 0.97$ .





Figure 26: Annealed high resolution ( $1024 \times 1024$ ) samples from FFHQ, with  $T = 0.97$ .



Figure 27:  $8\times$  super resolution on CelebA-HQ. The smaller images (top) are the original images at  $(128 \times 128)$ , while the larger images (bottom) are the annealed super resolution results  $(1024 \times 1024)$ , with  $T = 0.97$ .





Figure 28:  $8\times$  super resolution on FFHQ. The smaller images (top) are the original images at  $(128 \times 128)$ , while the larger images (bottom) are the annealed super resolution results  $(1024 \times 1024)$ , with  $T = 0.97$ .